https://doi.org/10.5194/egusphere-2025-1485
Preprint. Discussion started: 19 May 2025

GUST1.0: A GPU-accelerated 3D Urban Surface Temperature Model

Shuo-Jun Mei[1,2*], Guanwen Chen[1,2], Jian Hang[1,2], Ting Sun[3]

[1] School of Atmospheric Sciences, Sun Yat-sen University, and Southern Marine Science and Engineering Guangdong Laboratory (Zhuhai), Zhuhai 519082, PR China

[2] China Meteorological Administration Xiong'an Atmospheric Boundary Layer Key Laboratory, Xiong'an, P.R. China

[3] Department of Risk and Disaster Reduction, University College London, London, UK

Correspondence to: Shuo-Jun Mei (meishj@mail.sysu.edu.cn)

Abstract

The escalating urban heat, driven by climate change and urbanization, poses significant threats to residents' health and urban climate resilience. The coupled radiative-convective-conductive heat transfer across complex urban geometries makes it challenging to identify the primary causes of urban heat and develop mitigation strategies. To address this challenge, we develop a GPU-accelerated Urban Surface Temperature model (GUST) through CUDA architecture. To simulate the complex radiative exchanges and coupled heat transfer processes, we adopt Monte Carlo method, leveraging GPUs to overcome its computational intensity while retaining its high accuracy. Radiative exchanges are resolved using a reverse ray tracing algorithm, while the conduction-radiation-convection mechanism is addressed through a random walking algorithm. The validation is carried out using the Scaled Outdoor Measurement of Urban Climate and Health (SOMUCH) experiment, which features a wide range of urban densities and offers high spatial and temporal resolution. This model exhibits notable accuracy in simulating urban surface temperatures and their temporal variations across different building densities. Analysis of the surface energy balance reveals that longwave radiative exchanges between urban surfaces significantly influence model accuracy, whereas convective heat transfer has a lesser impact. To demonstrate the applicability of GUST, it is employed to model transient surface temperature distributions at complex geometries on a neighborhood scale. Leveraging the high computational efficiency of GPU, the simulation traces 10^5 rays across 2.3×10^4 surface elements in each time step, ensuring both accuracy and high-resolution results for urban surface temperature modeling.

https://doi.org/10.5194/egusphere-2025-1485
Preprint. Discussion started: 19 May 2025

1. Introduction

Urban overheating has become a pressing issue due to the combination effects of global warming, heatwaves, and rapid urbanization (Feng et al., 2023). The Urban Heat Island (UHI) effect is characterized by higher surface and air temperatures in urban areas than in surrounding rural areas, which exacerbates the urban overheating (Manoli et al., 2019). It is estimated that more than 1.7 billion people and 13,000 cities are facing urban overheating problems (Tuholske et al., 2021). Exposure to extreme urban heat poses a significant threat to residents' health, contributing to increased mortality and morbidity (Ebi et al., 2021). Identifying the main causes of hot urban surfaces is essential for developing effective strategies to mitigate urban overheating.

Physics-based models are powerful tools for uncovering the urban thermal balance and identifying the primary causes of urban heat (Carmeliet and Derome, 2024). They enable a quantitative evaluation of the contribution of each process, such as conduction, radiation, and convection, to the overall thermal balance. Urban surface temperatures are determined by the coupled heat transfer processes of conduction, radiation, and convection (Krayenhoff and Voogt, 2007). These heat transfer processes in urban areas differ from those in rural areas. First, urban materials typically have a lower heat capacity, allowing them to heat up more quickly and reach higher temperatures (Wang et al., 2018). Secondly, the complex three-dimensional geometry of urban environments leads to multiple reflections, which reduce urban albedo and limit the longwave heat loss to sky (Yang and Li, 2015). Thirdly, the densely packed buildings weaken the urban wind and thus reduce the convective transfer and further limit the heat loss (Wang et al., 2021).

A well-designed urban surface temperature model needs to accurately capture these heat transfer processes. Table 1 summarizes the models for urban surface temperatures and their schemes for conduction, radiation, and convection. For heat conduction, 1D models are commonly used due to the relatively thin walls of buildings in urban areas. For convective heat transfer, both parameterized convective coefficients and CFD (Computational Fluid Dynamics) simulations are commonly used. CFD simulations can better capture the spatial variations in air temperature in densely built urban areas, but the computational cost is much higher. The key distinction among these models lies in their radiation

https://doi.org/10.5194/egusphere-2025-1485
Preprint. Discussion started: 19 May 2025

schemes, as radiation is the primary energy input into the thermal system of urban surfaces. Moreover, simulating complex urban radiative transfer requires significant computational resources, necessitating simplifications and parameterizations to make the simulation more applicable.

Table 1 shows that the radiosity method is widely used to solve the reflections. In the radiosity method, the net longwave and shortwave radiation are solved by two main steps: 1) collecting luminous energy from both the sun and the sky vault, and 2) distributing the reflected energy based on view factors. The luminous energy is influenced by the shading pattern, which is solved by two main approaches in these models: 1) Sunlit-shaded distributions method, which employs ray tracing to determine whether a surface is illuminated; and 2) Flux reduction coefficients: where shading is accounted for by reducing the irradiance at shaded points. The reflection and longwave exchange between urban surfaces are determined by view factors, which can be calculated using three approaches: the analytical method, the discrete transfer method, and the Monte Carlo ray tracing method.

- **The analytical method** uses analytical solutions of view factors by assuming urban surfaces are composed of simple geometries.
- **The discrete transfer method (DTM)** uses ray tracing method to calculate view factors. The ray direction is determined by dividing the hemisphere into equal segments. This method counts the number of rays intersecting other surfaces.
- **The Monte Carlo Ray Tracing (MCRT)** is similar to DTM but differs by using rays that are directed randomly. This method is suitable for calculating view factors in complex geometries, but it requires a large number of rays.

The HTRDR-Urban adopted a different approach, using backward MCRT, to calculate the solar radiation considering multiple reflections (Schoetter et al., 2023). The Monte Carlo method (MCM) has been widely used to model solar radiation through the application of a ray tracing algorithm (Kondo et al., 2001). Recently, its application has been extended to address conduction, convection, and radiation problems (Villefranque et al., 2022). In backward MCRT, the energy of the incident light is divided into a large number of photons. By tracking the path of these photons and counting the number of photons absorbed, the net solar radiation reaching a given surface can be calculated. Tregan et al. (2023) proposed

https://doi.org/10.5194/egusphere-2025-1485
Preprint. Discussion started: 19 May 2025

a theoretical framework to solve linearized transient conduction-radiation problems with Robin's boundary condition in complex 3D urban geometry. Based on this framework, Caliot et al. (2024) developed a probabilistic model to simulate urban surface temperatures, using ray-tracing, walk-on-sphere and double randomization techniques. Their model leverages advancements in computer graphics for image synthesis and the Monte Carlo method (MCM), enabling it to effectively handle large and complex 3D geometries.

The advantage of MCM is its ability to handle complex geometries and albedos, while the disadvantage is its high computational cost. The low computational efficiency limits the application of MCM in real urban configurations. Although some models in Table 1 are validated against field measurements, others remain unvalidated. These models rely on various assumptions and parameterizations, and the lack of validation limits their accuracy. Additionally, using field measurement data to validate numerical models faces several challenges: 1) limited test points due to regulatory constraints and installation difficulties, 2) uncertainty in infrared imagery caused by varying view angles, and 3) heterogeneity in the optical and thermal properties of building materials.

This study aims to develop a GPU-based Urban Surface Temperature (GUST) model to enhance the computational speed of Monte Carlo Method. The absorption and reflection of longwave and shortwave radiation on outdoor surfaces modeled using the reverse Monte Carlo ray tracing (rMCRT) algorithm. The resulting shortwave and longwave radiation are then treated as heat flux boundary conditions for the 1D heat conduction model, which employs the Monte Carlo random walk method to calculate surface temperatures. High spatial-temporal resolution surface temperature data from a scaled measurement (SOMUCH) is employed to validate the parameterization and assumptions in this model.

The paper is organized as follows. Sect. 2 outlines the model structure and describes the algorithms used for the submodels. Sect. 3 presents the validation and evaluation of the model by comparing it with experimental data. Sect. 4 includes an example demonstrating how the model can be applied to complex geometries. Sect. 5 discusses the applications, limitations, and future development of the model. Lastly, Sect. 6 provides the conclusions.

https://doi.org/10.5194/egusphere-2025-1485
Preprint. Discussion started: 19 May 2025

Table 1. Overview of building-resolved models for urban surface temperature. The view factors are solved by both DTM (Discrete transfer method), analytical model, and Monte Carlo ray tracing method.

Model	**Solar Irradiation**	**Reflections and longwave exchange**	**Conduction**	**Convection**	**Validation**
HTRDR-Urban **(**Schoetter et al., 2023**)**	Backward Monte Carlo ray tracing	Backward Monte Carlo ray tracing	Monte Carlo random walking	Parameterized	N.A.
MUST (Yang and Li, 2013**)**	Sunlit-shaded distributions	Radiosity Method, DTM view factors	1D heat conduction	Parameterized	Thermal scanner and IRT (Voogt and Oke, 1998)
TUF-3D **(**Krayenhoff and Voogt, 2007**)**	Sunlit-shaded distributions	Radiosity Method, analytical view factors	1D heat conduction	Parameterized	Thermal scanner and IRT (Voogt and Oke, 1998)
SOLENE Microclimat **(**Imbert et al., 2018**)**	Sunlit-shaded distributions.	Radiosity Method, analytical view factors	1D heat conduction	Coupling CFD simulation	Thermographies measurement (Hénon et al., 2012)
Envi-Met **(**Eingrüber et al., 2024**)**	Flux reduction coefficients	Radiosity Method, DTM view factors	1D heat conduction	Coupling CFD simulation	Field measurements (Forouzandeh, 2021)
uDALES **(**Owens et al., 2024**)**	Sunlit-shaded distributions	Radiosity Method, DTM view factors	1D heat conduction	Coupling CFD simulation	N.A.
PALM (Resler et al., 2017**)**	Sunlit-shaded distributions	Radiosity Method, Analytical and DTM view factors	Empirical heat conductivity	Coupling CFD simulation	Field measurement (Resler et al., 2017)
MITRAS (Salim et al., 2018)	Meso-scale radiation scheme	Meso-scale radiation scheme (METRAS)	Force-restore method	Coupling CFD simulation	N.A.
OpenFOAM **(**Rodriguez et al., 2024**)**	Sunlit-shaded distributions	Radiosity Method, DTM view factor	1D heat-moisture diffusion.	Coupling CFD simulation	N.A.
FLUENT (Toparlar et al., 2015)	Sunlit-shaded distributions	Radiosity Method, DTM view factor	Shell conduction	Coupling CFD simulation	Field measurement (Toparlar et al., 2015)

https://doi.org/10.5194/egusphere-2025-1485
Preprint. Discussion started: 19 May 2025

2. Model design

GUST aims to resolve the urban surface temperature by a transient heat conduction model, as illustrated in Fig.1. The convective and radiative heat transfer at urban surfaces is treated as boundary conditions for the 1D heat conduction model. For the outdoor side, the heat flux (q_{out}) is the sum of radiative (longwave q_l and solar q_s) and convective heat flux ($q_{c,out}$).

$$q_{out} = q_l + q_s + q_{c,out} \tag{1}$$

The absorbed solar radiation, q_s is the sum of direct solar irradiation ($q_{s,o}$) and diffuse solar irradiation ($q_{s,r}$), expressed by: $q_s = q_{s,o} + q_{s,r}$. The longwave radiation flux q_l includes the radiation between urban surfaces ($q_{l,urban}$) and between urban surfaces and the sky ($q_{l,sky}$), represented as $q_l = q_{l,urban} + q_{l,sky}$.

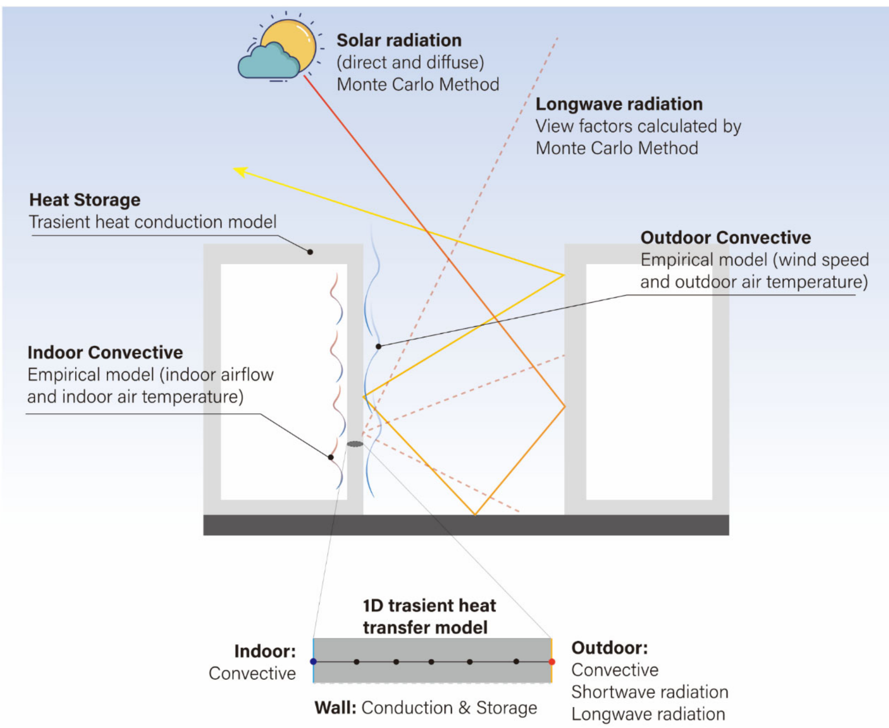

Figure 1: The model design of GUST. In this model, 1D transient conductive heat transfer is considered for urban surfaces the system (e.g., walls, roofs, and ground). They are composed of multiple layers where the

https://doi.org/10.5194/egusphere-2025-1485
Preprint. Discussion started: 19 May 2025

thermal properties are uniform and isotropic. All urban surfaces are assumed to be opaque in this study.

2.1. Conduction sub-model

The Monte Carlo random walking method is used to solve the 1D heat conduction (Talebi et al., 2017). Compared to finite volume method, this approach is insensitivity to the complexity of urban geometry and boundary conditions (Villefranque et al., 2022; Caliot et al., 2024). In the present version, the heat conduction along the wall span is neglected. The one-dimensional (1D) transient heat conduction equation is:

$$\frac{\partial}{\partial t}T = \alpha \frac{\partial^2 T}{\partial x^2} \tag{2}$$

where $\alpha = \frac{k}{\rho c_p}$ is the solid thermal diffusivity and k the thermal conductivity, ρ the density, c_p the specific heat capacity. The ground, walls and roofs are composed of multiple layers. In the Monte Carlo random walking method, the heat conduction equation is replaced by finite difference approximation as:

$$T(x, t + \Delta t) = P_t T(x, t) + P_{x-} T(x - \Delta x, t + \Delta t) + P_{x+} T(x + \Delta x, t + \Delta t) \tag{3}$$

where $P_t = \frac{1}{1+2Fo}$ is defined as probability of time step; $P_{x-} = P_{x+} = \frac{Fo}{1+2Fo}$. where P_{x-} and P_{x+} respectively represent the probabilities of stepping to the points $(x - \Delta x, t)$ and $(x + \Delta x, t)$. Here, $Fo = \frac{k\Delta t}{\rho c_p (\Delta x)^2}$ These coefficients are nonnegative probabilistic values and

$$P_t + P_{x-} + P_{x+} = 0 \tag{4}$$

The Monte Carlo random walking algorithm is schematically illustrated in Fig. 2. The core idea is that particles walk by following rules:

1) Start a random walk at point *x*.

2) Generating a random number (R) between 0 and 1.

3) Determine walking direction by conditions

https://doi.org/10.5194/egusphere-2025-1485
Preprint. Discussion started: 19 May 2025

$$\begin{cases} 0 < R < P_{x-}: & x \to (x - \Delta x) \\ P_{x-} < R < (P_{x-} + P_{x+}): & x \to (x - \Delta x) \\ (P_{x-} + P_{x+}) < R: & x \to (x), T(i) = T(i) + T(x, t - \Delta t) \end{cases} \tag{5}$$

4) If the next point is not on the boundary repeat step 2 and 3 and if it is on the boundary, record $T(i) = T(i) + T$ at the boundary and go to step 1.

5) After N random walking, temperature at point x is calculated by

$$T(x) = \frac{T(i)}{N} \tag{6}$$

When a particle reaches a heat flux, convective or interface boundary, its movement follows the following rules.

1) Heat flux boundary

When the particle walks to the boundary of heat flux (q), it is bounced back and record the temperature T_{hf}, which is calculate by $T_{hf} = \frac{q\Delta x}{k} + \frac{q}{2k}(\Delta x)^2$.

2) Convective boundary

The heat flux of a convective boundary is calculated by $q = h(T_w - T_a)$, where h is the heat transfer coefficient and T_w the wall temperature and T_a the air temperature. The wall temperature is calculated by

$$T_w = \frac{1}{1 + Bi} T(x - \Delta x) + \frac{Bi}{1 + Bi} T_a \tag{7}$$

Where $P_x = \frac{1}{1+Bi}$, $P_a = \frac{Bi}{1+Bi}$, $Bi = \frac{h\Delta x}{k}$. When the particle reaches the convective boundary, a new random number R was generated and moves as follows:

$$\begin{cases} 0 < R < P_x: & \to \text{bounced back} \\ P_x < R < 1: & \to \text{absorbed by air with } \mathrm{T(i)} = \mathrm{T(i)} + T_a \end{cases} \tag{8}$$

3) Interface between two layers

The interface between layers is flux continuity, i.e. the conductive fluxes are equal on both sides of the interface. The heat conductivities on left and right sides of the interface are k_A and k_B. The conductive

https://doi.org/10.5194/egusphere-2025-1485
Preprint. Discussion started: 19 May 2025

heat fluxes on both sides are equal, i.e., $-k_A \frac{dT}{dx} = -k_B \frac{dT}{dx}$. When a particle reaches the interface, it may be reflected or move to the next layer. A new random number R is generated. The particle moves by following

$$\begin{cases} 0 < R < P_{x-}: & \rightarrow \text{bounced back to layer A} \\ P_{x-} < R < 1: & \rightarrow \text{move to layer B} \end{cases} \tag{9}$$

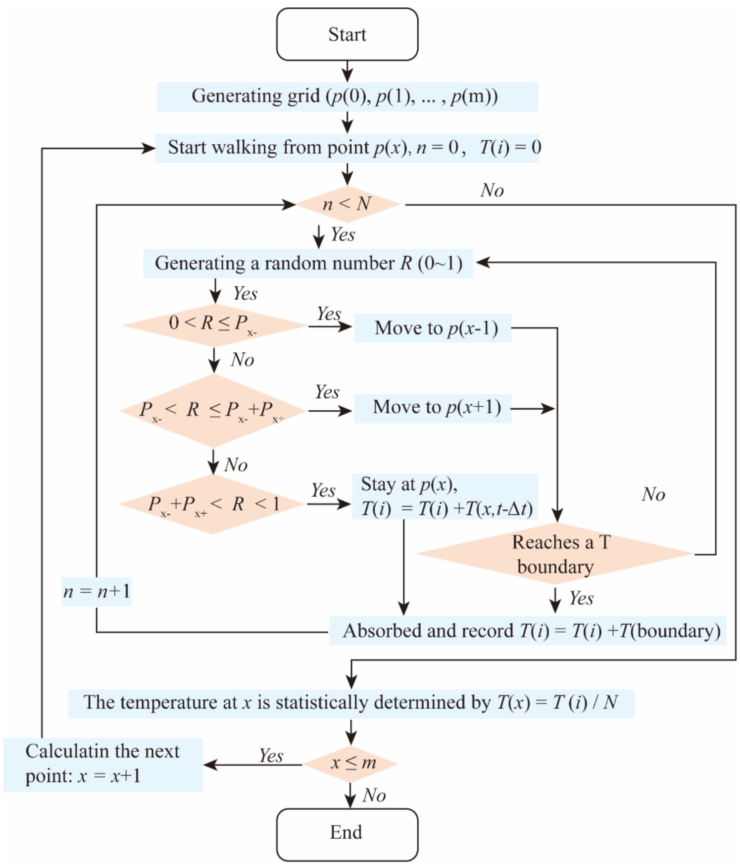

Figure 2: Flowchart of the Monte Carlo random walking algorithm for 1D heat conduction. At each point, the particle movement stops after N random walks. Each walk stops when particle either reaches a fixed temperature boundary or remains stationary. Orange diamonds indicate decision points with two possible outcomes (Yes/No).

https://doi.org/10.5194/egusphere-2025-1485
Preprint. Discussion started: 19 May 2025

2.2. Solar radiation sub-model

The reverse Monte Carlo Ray Tracing (rMCRT) method is used to calculate the solar radiation q_s and longwave radiation q_l. The ray starts from the target points, instead of starting from the sky or sun in the ray tracing method (Caliot et al., 2024). This method ensures that enough photons reach the target point to obtain a statistical result.

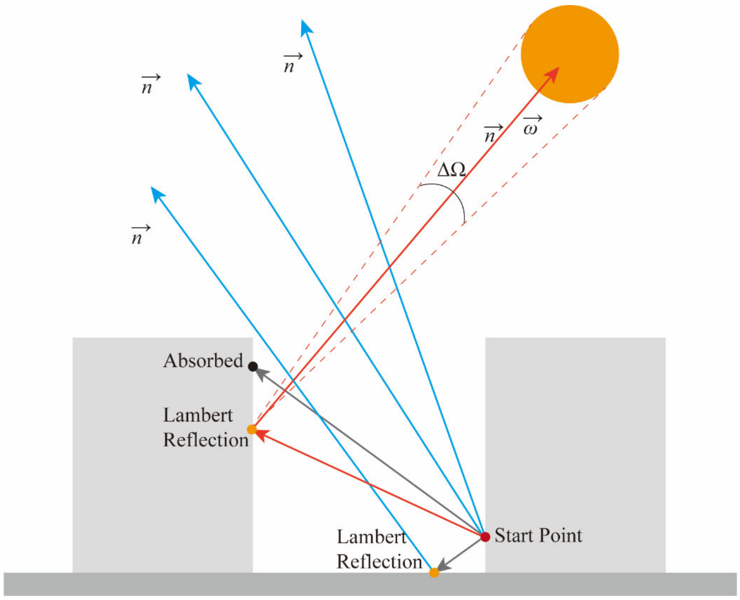

Figure 3: Schematic illustration of the reverse MCM ray tracing method for calculating the directional and diffuse solar radiation.

The procedure of reverse MCM is schematically explained in Fig. 3. In total, N photons leave the target point in random directions ($\vec{r}$), which is determined by the azimuth θ_a and incidence angle η_a. These angles are calculated by $\theta_a = 2\pi R_1$ and $\eta_a = \arccos(1 - 2R_2)$, where R_1 and R_2 are random numbers between 0 and 1.

When a photon reaches the surface, it can be absorbed or reflected via Lambert's law. To determine whether this photon is absorbed, a random number R_{ab} (ranging from 0 ~ 1) is generated. When $R_{ab} > \alpha_s$ (surface albedo), the photon is absorbed by the surface. When $R_{ab} < \alpha_s$, the photon is reflected. All surfaces are considered Lambertian and the direction of reflect solar beam is determined by the azimuth

https://doi.org/10.5194/egusphere-2025-1485
Preprint. Discussion started: 19 May 2025

θ_a and incidence angle η_a of that surface. At each reflection, θ_a and η_a are recalculated by regenerating new random numbers.

When the photon reaches the "sky" in the direction of $\vec{r}$, its angle (θ_{ns}) with the reverse solar direction $\overrightarrow{\omega_{sun}}$ is calculated. When $\theta_{ns} < \Delta\Omega_d$, that photon is marked as reaching the "Sun", otherwise, that photon is marked as reaching the "Sky". The direct ($q_{s,o}$) and diffuse ($q_{s,r}$) solar radiation reaching the target point can then be statistically determined by:

$$q_{s,o} = \frac{\pi I_{s,o}}{\Delta\Omega_d N} \sum_{\theta_{ns}<\Delta\Omega_d} \left|\vec{\omega}_{sun} \cdot \vec{n}\right| \tag{10}$$

$$q_{s,r} = \sum_{\theta_n > d\Delta\Omega_d} \frac{I_{s,r}}{N} \tag{11}$$

where $I_{s,o}$ and $I_{s,r}$ is the downward direction and diffuse solar radiation. The ratio between the directional and diffuse solar radiation is calculated by the model proposed by (Reindl et al., 1990).

The rMCRT requires a large number of rays to achieve statistically reliable results. To accelerate the simulation, the model is run in parallel on GPUs (Graphics Processing Units) using the CUDA® platform (Yoshida et al., 2024). The advantage of GPUs is that they have a large number of cores, which enables them to handle many parallel tasks simultaneously. GPUs are particularly well-suited for accelerating MCRT, since each ray tracing operation is independent.

The GPU parallel computing is executed using two strategies, based on the number of elements and points. As illustrated in Fig. 4, Strategy 1 calculates the radiative flux point by point, emitting n photons for ray tracing simulation. Each photon is processed in a separate GPU core. Once the ray tracing process is complete, the results from the GPU cores are copied to the CPU, where radiative flux at each point is calculated. Strategy 2 calculates the radiative flux for all points simultaneously, with each GPU core computing the flux for a single point. The ray tracing of n photons is performed iteratively on the GPU.

The advantage of Strategy 1 is the efficient utilization of GPU cores when the number of points and elements is small. However, its disadvantage is that it requires a large amount of memory when the number of points is large. In contrast, Strategy 2 requires significantly less memory and only transfers data to the CPU once, making it highly efficient when the number of points and elements is large.

https://doi.org/10.5194/egusphere-2025-1485
Preprint. Discussion started: 19 May 2025

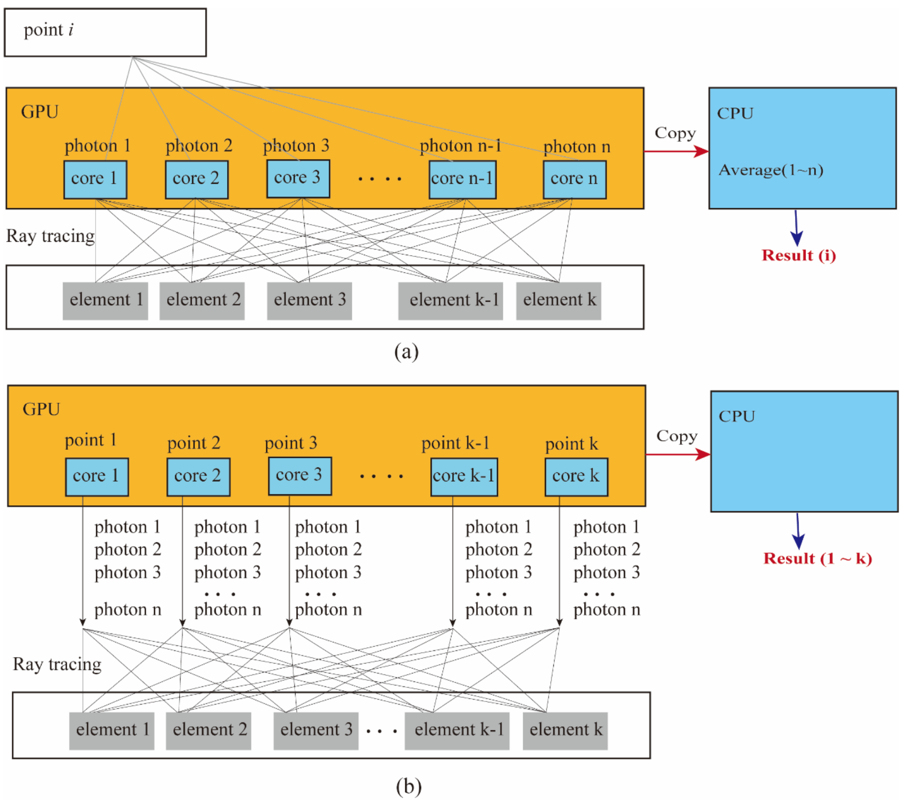

Figure 4: Two strategies for GPU parallel computing. (a) The ray tracing is conducted point by point. For each point, n photons are emitted. Each GPU core calculates one photon. (b) The ray tracing is conducted for all points at one time. Each GPU core calculates one point. The ray tracing of n photons is performed iteratively within the GPU core.

The space angle of the Sun ($\Delta\Omega_d$) and the number of photons (N) can significantly affect the accuracy of reverse MCM. To evaluate this influence, a series of test cases are conducted, in which the directional solar radiation at a ground point is calculated. The solar radiation on the open ground can be calculated theoretically, as there is no shading from buildings.

Figure 5 shows the errors of simulations using different values of N and $\Delta\Omega_d$. The simulation time of each case is also indicated in that figure. When the number of photons is increased from $N = 10^5$ to $N = 10^7$, the simulation time increases from 0.05s to 1.15s, which is an increase of 23 times. The

https://doi.org/10.5194/egusphere-2025-1485
Preprint. Discussion started: 19 May 2025

relatively slow increase in simulation time is a result of the parallel computing capabilities of the GPU. In each scenario, the model was run 20 times to observe the difference between each run.

A small $\Delta\Omega_d$ reduce the photon number reaching the Sun, thus increasing the error, where the $\Delta\Omega_d$ is calculated from a 2D angle θ as $\Delta\Omega_d = 2\pi(1-\cos(\theta))$. For example, the error in cases with $\theta = 3°$ greater than that in cases with $\theta = 6°$. A larger number of photons is needed to compensate for this error. For example, the case with $\theta = 3°$ and $N = 10^7$ shows acceptable accuracy. However, the case with $\theta = 6°$ shows a comparable accuracy when $N = 10^6$ and takes less simulation time.

In the subsequent simulations, $\theta = 6°$ and $N = 10^6$ are applied to balance accuracy and simulation time.

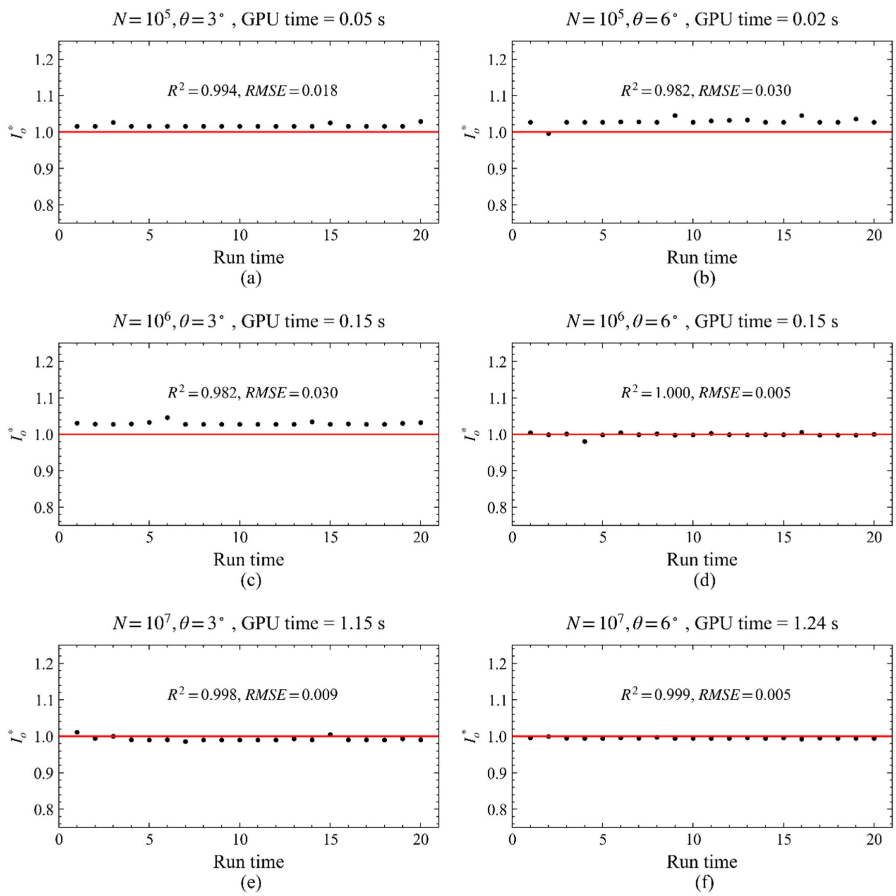

https://doi.org/10.5194/egusphere-2025-1485
Preprint. Discussion started: 19 May 2025

Figure 5: Numerical errors of directional solar radiation estimation using Monte Carlo method. The simulated solar radiation ($I_{o,sim}$) is normalized by the true value ($I_{o,true}$) and is expressed by ($I_o^* = \frac{I_{o,sim}}{I_{o,true}}$), where $I_o^* = 1.0$ represents an exact reproduction of the solar radiation. The test cases use different space angles of sun $\Delta\Omega_d = 2\pi(1-\cos(\theta))$ and photon numbers (N). The red lines represent the true value, and dots represent the simulated data.

2.3. Longwave radiation sub-model

The view factors between the surfaces, as well as from the surfaces to the sky, are also calculated using the Monte Carlo ray tracing model, as illustrated in Fig. 6. The urban surfaces are divided into multiple triangular elements N_{ur}. The view factor from element S_i to element S_j, denoted as $F_{i,j}$, is calculated by emitting N photons from the centroid of element S_i. The algorithm then counts the number of photons $n_{i,j}$ that reach element S_j. Finally, the view factor $F_{i,j}$ is calculated by $F_{i,j} = n_{i,j}/N$. The sky view factor is also determined in this approach by treating the sky as an urban surface.

The longwave radiative heat exchange between the surfaces, as well as from the surfaces to the sky, is calculated by:

$$q_l = F_{i,sky}\varepsilon(R_{l.in} - \sigma T_i^4) + \varepsilon\sigma \sum_{j=1}^{j=N_{ur}} F_{i,j}\left(T_j^4 - T_i^4\right) \quad (12)$$

where ε is the material emissivity, σ is Stefan–Boltzmann constant (= 5.67 × 10^{-8}) (W m^{-2} K^{-1}), $R_{l.in}$ is the downward longwave radiation from the sky, $F_{i,sky}$ is the sky view factor of element S_i. The surface temperature from the previous step (T_i and T_j) is used to calculate the longwave radiative heat exchange.

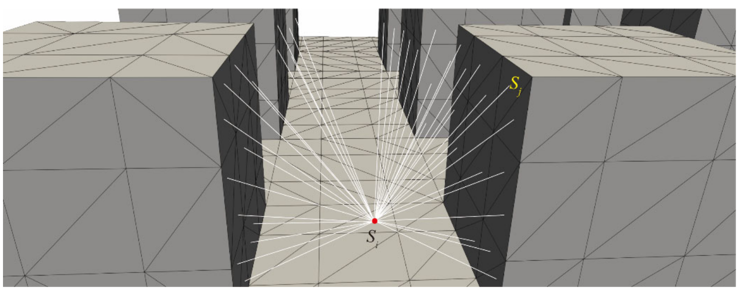

Figure 6: Schematic illustration of how view factors are calculated between urban surface elements.

https://doi.org/10.5194/egusphere-2025-1485
Preprint. Discussion started: 19 May 2025

2.4. Outdoor convective sub-model

GUST does not calculate urban airflow; instead, it uses empirical formulas to calculate the outdoor convective heat flux as follows:

$$q_{c,out} = U_f h_{out}(T_{w,out} - T_{a,out}) \tag{13}$$

where $T_{a,out}$ is the outdoor air temperature in the canopy layer, U_f is the wind speed, and convective heat transfer coefficient $h_{out} = 4.5 \left(\frac{Ws}{\mathrm{m^3 K}}\right)$ is adopted.

The wind speed above the urban canopy layer (UCL) is calculated by a logarithm wind profile:

$$U(z) = \frac{u_*}{\kappa} \ln\left(\frac{z + z_0}{z_0}\right) \tag{14}$$

where z_0= 0.1H based on the estimation of (Grimmond and Oke, 1999).

The wind speed within the UCL is assumed to be uniform and is calculated by the model by Bentham and Britter (Bentham and Britter, 2003). This model estimates the in-canopy velocity (U_c) based on the frontal area density (λ_f) as follows:

$$\frac{U_c}{u_*} = \left(\frac{2}{\lambda_f}\right)^{0.5} \tag{16}$$

Here, the friction velocity (u_*) depends on the urban morphology and is estimated using the following functions (Yuan et al., 2019):

$$\begin{cases} u_* = 0.12U_{2H}, & \text{for } (\lambda_f > 0.4) \\ u_* = 6.7U_{2H}^3 - 6.4U_{2H}^2 + 1.7U_{2H} + 0.03, & \text{for } (\lambda_f < 0.4) \end{cases} \tag{17}$$

where U_{2H} is the wind speed at a height of 2H above the ground, and H is the building height.

The air temperature in UCL is assumed to be uniform and calculated by the urban canopy model (Yuan et al., 2020). This model estimates the in-canopy temperature based on the exchange velocity U_E and sensible heat flux $q_{c,out}$.

$$T_c = \frac{1}{D_c} \frac{q_{c,out}}{U_{2H}(1 - \lambda_p)} \left(1 - 0.12\left(\frac{2}{\lambda_f}\right)^{0.5}\right) + T_{a,2H} \tag{18}$$

https://doi.org/10.5194/egusphere-2025-1485
Preprint. Discussion started: 19 May 2025

where D_c = 17.183, is a heat capacity constant of the air, $T_{a,2H}$ is the air temperature above the roof level, λ_p is the plan area density. Bentham and Britter (Bentham and Britter, 2003) suggested that the U_E can be calculated by:

$$\frac{U_E}{u_*} = \left(\frac{U_{2H} - U_c}{u_*}\right)^{-1} \tag{19}$$

The $q_{c,out}$ is calculated by the temperature from previous time step.

2.5. Indoor sub-model

The indoor side uses a convective boundary condition given by $q_{in} = h_{in}(T_{w,in} - T_{a,in})$, where $T_{a,in}$ is the indoor air temperature, $T_{w,in}$ is the wall temperature on indoor side. The indoor heat transfer coefficient $h_{in} = 13.5\frac{\mathrm{W}}{\mathrm{m^2K}}$ accounts for both natural convection and longwave radiative heat flux.

For air-conditioned rooms, the indoor air temperature is assumed to be constant at $T_{\mathrm{a,in}}$ = 26 °C. In contrast, for naturally ventilated rooms, the indoor air temperature is assumed to be equal to the in-canopy air temperature, represented as $T_{\mathrm{a,in}} = T_{\mathrm{c}}$.

3. Model validation and assessment

3.1. SOMUCH measurement

The model is validated by cross-compare with the SOMUCH measurement, which is a scale outdoor field measurement conducted in Guangzhou, P.R. China (23°1′ N, 113°25′ E) (Hang and Chen, 2022; Hang et al., 2025; Wu et al., 2024). This measurement provides a quality database for evaluating urban climate models (Hang et al., 2024; Chen et al., 2025). The campaign conducted from 29th Jan to 1st Feb 2021 is used. In that campaign, both surface and air temperatures were measured at high resolution, making it an ideal database for validating current models.

The geometry of the building blocks and measurement points are plotted in Fig. 7. In that measurement, the urban buildings are modeled by hollow concrete blocks with a size of 0.5 m× 0.5 m× 1.2 m and a thick of 0.015 m. The blocks are arranged to form street canyons with four different aspect ratios, i.e., H/W = 1, 2, 3, 6. Each row consists of 24 blocks and has a length of L = 12 m. In the experiment, the surface and air temperatures are measured using thermocouples (Omega, TT-K-36-SLE, Φ0.127 mm and

https://doi.org/10.5194/egusphere-2025-1485
Preprint. Discussion started: 19 May 2025

TT-K- 30-SLE, Φ0.255 mm). The wind speeds inside and above the street canyon are measured using sonic anemometers (Gill WindMaster). The incoming longwave and shortwave radiation are measured using weather stations (RainWise PortLog). The thermal characteristics of the concrete and ground are listed in Table 1.

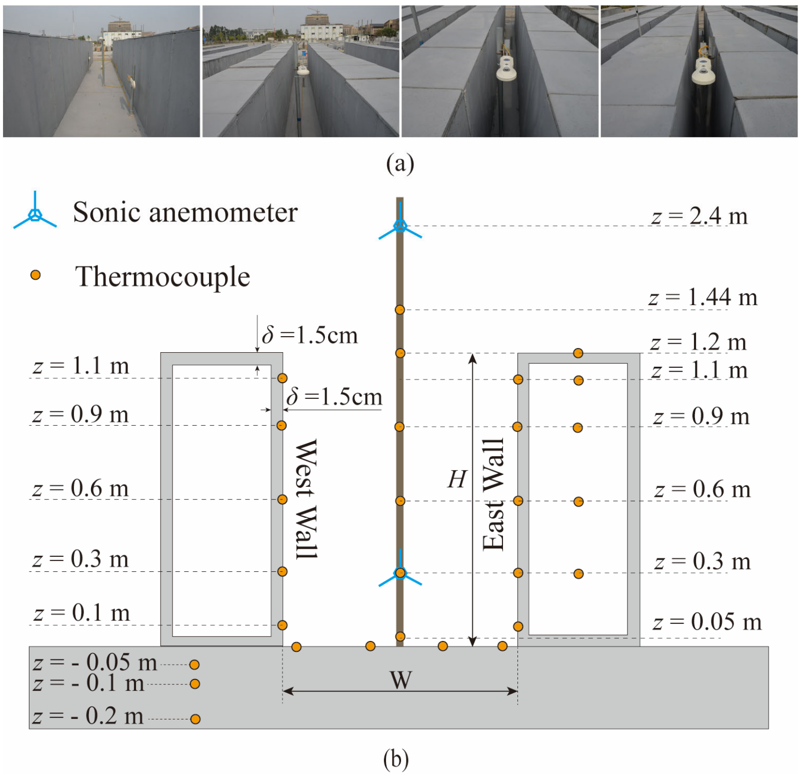

Figure 7: Photograph of the SOMUCH experiment (a). The geometry of concrete blocks and measurement points in SOMUCH (b). The thermocouples are used to measure the surface temperature and air temperature. The sonic anemometers are used to measure wind speed.

https://doi.org/10.5194/egusphere-2025-1485
Preprint. Discussion started: 19 May 2025

Table 2. Thermal properties of the building material. The emissivity is for the longwave radiation and albedo is for the shortwave radiation.

Material	Density $\boldsymbol{\rho}$ (kg m^{-3})	Conductivity $\boldsymbol{k}$ (W m^{-1} K^{-1})	Specific Heat Capacity $\boldsymbol{c_p}$ (J kg^{-1} K^{-1})	Emissivity $\boldsymbol{\varepsilon}$	Albedo $\boldsymbol{\alpha}$
Concrete	2420	2.073	618	0.87	0.24

3.2. Cross comparison of the roof temperature

The surface temperature model is validated by cross-comparing with SOMUCH measurement. Many factors affect the accuracy of the model, including the radiation, convective and conduction. To separately investigate these factors, the temperatures at roofs are first validated because the total radiative flux of roof is only influenced by the incoming longwave and shortwave radiation. The shading effect of other blocks can be ignored as the block heights are uniform. Therefore, the accuracy of conductive and convective sub-models can be separately evaluated.

The accuracy of this model is quantitatively evaluated by two statistical parameters, the root mean square error (RMSE), and coefficient of determination (R^2). The RMSE and R^2 of u_x^* are calculated by:

$$\mathrm{RMSE} = \sqrt{\frac{1}{n}\sum_{i=1}^{n}(O_i - P_i)^2} \tag{21}$$

$$\mathrm{R}^2 = 1 - \frac{\sum_{i=1}^{n}(O_i - P_i)^2}{\sum_{i=1}^{n}\left(O_i - \overline{O_i}\right)^2} \tag{22}$$

where O_i represents the measured values, P_i is the simulated values, $\overline{O_i}$ is the mean of the measured values, and n is the number of data points.

The wind speed at roof level is needed to calculate the outdoor convective flux of roofs. In SOMUCH measurement, the wind speed was measured above the roof and at a height of $2H$. The wind speed at roof level is estimated by a logarithm wind profile as:

https://doi.org/10.5194/egusphere-2025-1485
Preprint. Discussion started: 19 May 2025

$$U(z) = \frac{u_*}{\kappa} \ln\left(\frac{z + z_0}{z_0}\right) \quad (23)$$

where $z_0 = 0.1H$ based on the estimation of (Grimmond and Oke, 1999). The wind velocity at roof level ($z = H$) can be calculated by $\frac{U_H}{U_{2H}} = 0.787$. The outdoor air temperature, incoming shortwave and longwave radiation, are from the weather station ($z = 2H$).

For the indoor side, the radiative flux between indoor surfaces is ignored in this model. Only the convective flux is modeled. The convective velocity is assumed to be 3 m/s and CHTC is assumed to be 4.5 for indoor side. Data from the indoor measurement point at $H = 1.1$ m is used. That point is the nearest measurement point to the roof.

Figure 8(a) plotted the measurement data that was used to drive the model. Fig. 8(b) shows the roof surface temperatures from measurement and simulation. Generally, the roof surface temperatures are well reproduced by the model, because the R^2 is 0.99 and $RMSE$ is 1.28. The large discrepancy is found around noon. The model slightly overestimates the roof temperature. The comparison of roof temperatures shows that the conductive and convective sub-models are reliable.

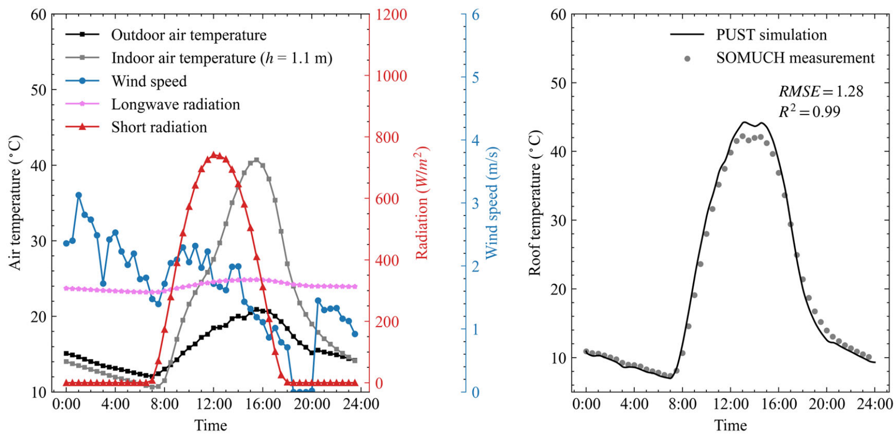

(a) (b)

Figure 8: The weather data on the measurement date (measured on 29th Jan 2021) is plotted in (a). Comparison of the roof surface temperatures from simulation and measurement (b). The points represent measured data and lines represent the simulated data.

https://doi.org/10.5194/egusphere-2025-1485
Preprint. Discussion started: 19 May 2025

3.3. Cross comparison of the wall temperature

The temperatures at walls are more complicated than those at the roof because the buildings change the radiative fluxes and wind speeds in street canyons. The radiative fluxes need to be accurately modelled as they are the main energy input and have a large impact on the surface temperature. To avoid the influence of air temperature and wind speed modeling, the canyon air temperature, wind speed, and indoor temperature are from the measurement. The air temperatures are measured from multiple heights. For the convective flux modelling, the nearest measured air temperatures are used. The wind speeds from the sonic anemometer in the street canyon (z = 0.3 m) are used to calculate the convective flux at outdoor side. The driving data are plotted in Appendix A.

The east and west walls are defined by taking street canyon center as the origin point. The street direction is tilted from north toward east by 25°. Therefore, the west and east walls are roughly defined to distinguish them. The street orientation has been modeled in our model and will not cause additional discrepancy.

Figure 9 shows the comparison of wall temperatures from simulation and measurement. The R^2 and RMSE are calculated and marked in each sub-figure. Generally, the wall temperatures are well reproduced, particularly their variation trend. The peak hours are well reproduced. For example, there are two temperature peaks for the west wall. The first one is around 10:00 and the second is around 16:00. Both simulation and measurement show the same occurring time. The accuracy of wall temperature modeling varies from point to point. There are two main observations from the comparison of wall temperatures.

a) Accuracy Difference Between Walls: The temperatures on the east wall are modeled more accurately than those on the west wall, as the model tends to underestimate the peak temperatures on the west wall. For H/W = 1, the R^2 values for west wall temperatures range from 0.95 to 0.98, while those for east wall temperatures range from 0.91 to 0.95. For H/W = 2, the R^2 values for the west and east wall temperatures show only a slight difference. However, the RMSE values for the west wall, which range from 0.69°C to 1.85°C, are evidently lower than those for the east wall, which range from 0.82°C to 2.53°C. The R^2 and RMSE values for H/W = 3 are comparable to those for H/W = 2.

https://doi.org/10.5194/egusphere-2025-1485
Preprint. Discussion started: 19 May 2025

b) Accuracy Difference Between Points: The underestimation of west wall temperature particularly pronounced at higher levels (z = 90 cm and 110 cm). At lower levels (z = 10 cm and 30 cm), temperatures are underestimated at night. The largest discrepancies occur at these lower levels in *H/W* = 6, with a minimum R^2 of 0.51 and a maximum RMSE of 1.98°C. The R^2 values suggest that wall temperatures at these levels are estimated poorly; however, the RMSE values do not appear abnormally high, reaching 2.53 °C at z = 90 cm in *H/W* = 2. The main reason for this discrepancy is that wall temperatures in deep street canyons (*H/W* = 6) show only a slight increase compared to the air temperature, due to minimal sunlight penetration into the canyon. In these cases, wall temperatures can be highly sensitive to convective and longwave radiative fluxes.

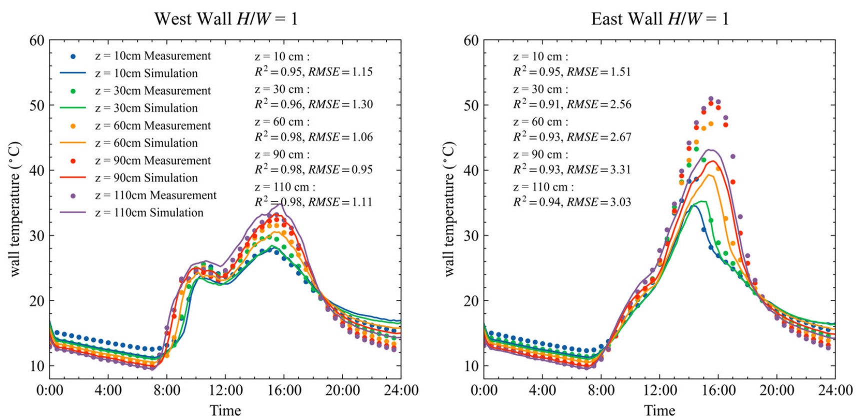

(a) *H/W* = 1

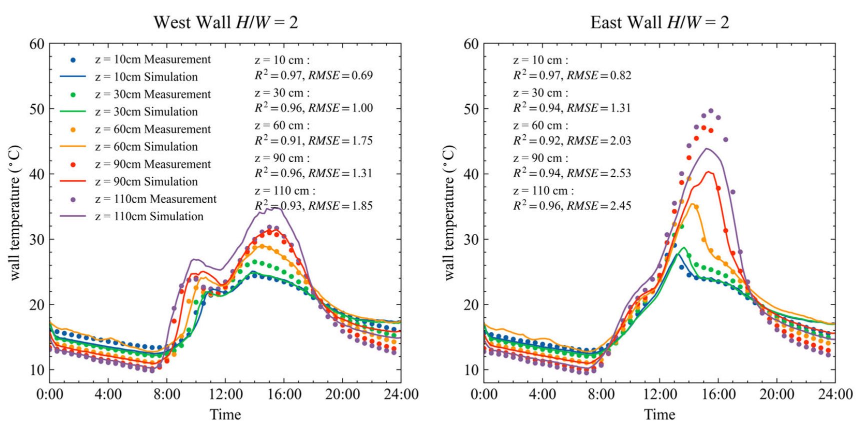

https://doi.org/10.5194/egusphere-2025-1485
Preprint. Discussion started: 19 May 2025

(b) *H/W* = 2

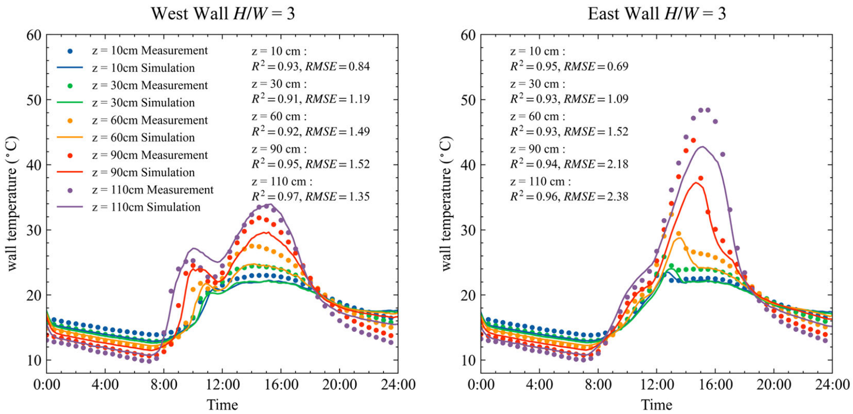

(c) *H/W* = 3

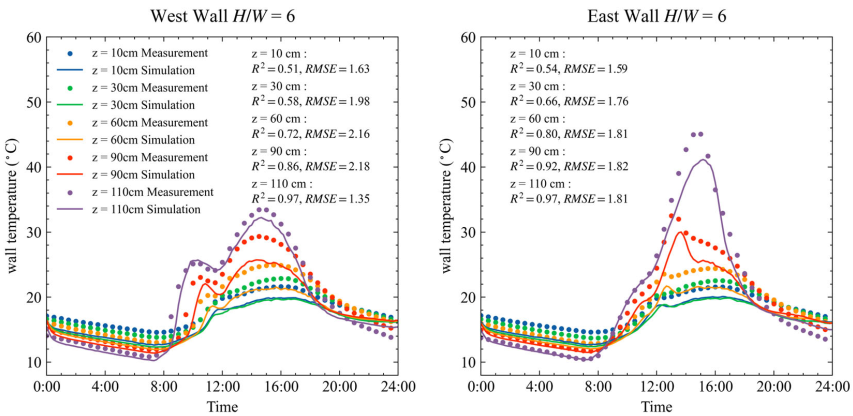

(d) *H/W* = 6

Figure 9: Wall temperature comparison between the simulation and measurement results at street canyon aspect ratio of *H/W* = 1.0, 2.0, 3.0, and 6.0. Surface temperatures are measured on 29th Jan 2021. The root mean square error (RMSE), and coefficient of determination (R^2) are calculate and plotted. The points represent measured data and lines represent the simulated data.

https://doi.org/10.5194/egusphere-2025-1485
Preprint. Discussion started: 19 May 2025

3.4. Cross comparison of the ground temperature

The surface temperatures of the ground are heavily influenced by heat storage. During the day, heat is conducted to deeper layers and stored there. At night, this stored heat is released. Therefore, the initial temperature field and boundary conditions are critical for accurately modeling surface temperatures. In this study, an adiabatic boundary condition is applied at a depth of 0.5 m below the ground surface. The soil material is divided into three layers with thicknesses of 0.2 m, 0.15 m, and 0.15 m. All three layers are assumed to be made of concrete. The thermal properties in Table 1 are used. The underground temperatures are measured by thermocouples with three depths of 5 cm, 10 cm, and 20 cm, as plotted in Appendix A. In this study, we used only the measured underground temperatures at 0:00 to initialize the underground temperature field. It is important to note that the available soil temperatures were measured in open ground rather than under street canyons. This difference may lead to discrepancies in modeling ground surface temperatures.

Figure 10 shows the ground surface temperatures from measurement and simulation. The ground surface temperatures are measured at four locations: g1, which is close to west wall; g4, which is close to east wall; and g2 and g3, which are situated in the middle of the streets. Generally, the temperature variations are well reproduced by the model. For example, peak temperatures occur sequentially from g1 to g4 due to the movement of the building's shadow. This phenomenon is observed in both simulations and measurements.

The accuracy of ground temperatures is lower than that of the wall temperatures in terms of R^2. For example, in $H/W = 2$, the R^2 values for temperatures at the west wall range from 0.91 to 0.97, while those at the ground range from 0.64 to 0.89. However, the ground temperatures can be considered better modeled because the RMSE for ground temperatures is smaller than that for wall temperatures. Using $H/W = 2$ as an example, the RMSE values for the west wall range from 0.69 to 1.85 °C, while those for the ground range from 1.05 to 1.24 °C. This difference between the R^2 and RMSE values is due to the ground temperature increase being much lower than that of the walls because of shading, particularly in deep street canyons.

Uncertainties in the input data may also contribute to the discrepancies between simulation and

https://doi.org/10.5194/egusphere-2025-1485
Preprint. Discussion started: 19 May 2025

measurement. First, the thermal properties of soil can differ significantly from those of concrete blocks. Secondly, the initial temperature is measured in surrounding area, rather than in street canyons. Thirdly, since the same initial temperature field is used for all four points, the model is unable to reproduce the differences between points at night.

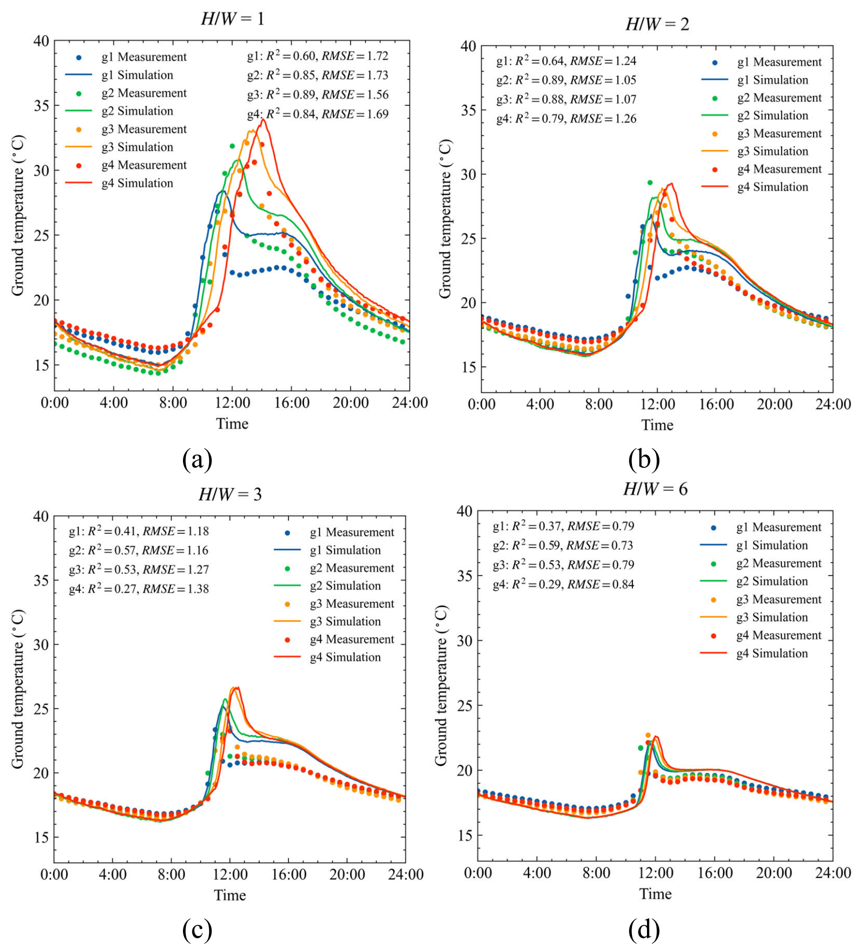

Figure 10: Ground temperature comparison between the simulation and measurement results at street canyon aspect ratio of *H/W* = 1.0, 2.0, 3.0, and 6.0. Surface temperatures are measured on 29th Jan 2021. The root mean square error (RMSE), and coefficient of determination (R^2) are calculate and plotted. The points represent measured data and lines represent the simulated data.

https://doi.org/10.5194/egusphere-2025-1485
Preprint. Discussion started: 19 May 2025

3.5. Surface energy balance analysis

The surface temperature comparison indicates that model uncertainties arise from various factors. To identify the main factors impacting the model accuracy, the energy balance of wall surface is analyzed. The heat fluxes of shortwave (Q_K), longwave radiation (Q_L), convection (Q_H), and conduction (Q_G) of outer surface of walls satisfy the following equation:

$$Q_K + Q_L + Q_G + Q_H = 0 \tag{24}$$

Here, the longwave heat flux Q_L is divided into two parts as the heat exchange between wall to sky ($Q_{L,sky}$) and to other urban surfaces ($Q_{L,urban}$), expressed as $Q_L = Q_{L,sky} + Q_{L,urban}$. This analysis aims to determine whether it is necessary to model the longwave heat exchange between urban surfaces, which requires substantial computational resources.

Figure 11 shows the heat fluxes of walls in the simulation. The heat fluxes of east and west walls are averaged from five measurement points on each. Our previous study has demonstrated that the Monte Carlo ray tracing method has good accuracy in predicting solar radiation.

In all cases, longwave radiative heat exchange between urban surfaces plays an important role in the energy balance, particularly at high aspect ratios. The longwave radiative fluxes from sky only contribute a small amount of total longwave radiative flux in *H/W* = 6, as shown in Fig. 10(d). The shading effect of buildings creates heterogeneous surface temperatures within the urban canopy layer. The large temperature differences between surface elements contribute a large portion of the total heat flux. This highlights the necessity for accurate modeling of longwave heat exchange between urban surfaces, even though it demands significant computational resources.

The conductive heat flux also contributes a large portion of the total heat flux. It is negative in the morning and positive in the afternoon, meaning that heat is stored in the building block during the morning and released in the afternoon. In the reduced scale experiment, buildings were represented by airtight hollow concrete blocks. Due to the lack of ventilation, the indoor air temperature can rise to 40°C under an outdoor air temperature of 20°C, as shown in Appendix A. This indicates that the indoor air can also absorb, store, and release a considerable amount of heat. Therefore, accurately modeling indoor

https://doi.org/10.5194/egusphere-2025-1485
Preprint. Discussion started: 19 May 2025

air temperature is essential for effective surface temperature modeling.

The convective contributes a smaller amount of the total heat flux. In high aspect ratio cases (H/W = 3 and 6), the convective heat fluxes are almost negligible. This is due to the weak wind in the deep street canyons. In this model, the surface convective heat flux is directly calculated from the wind speeds in street canyons. This assumption may underestimate the convective flux, especially since natural convection occurs under weak wind conditions (Fan et al., 2021).

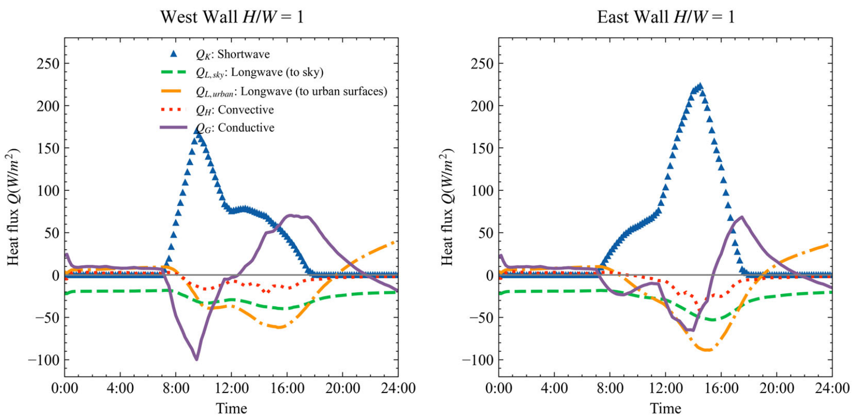

(a) $H/W = 1$

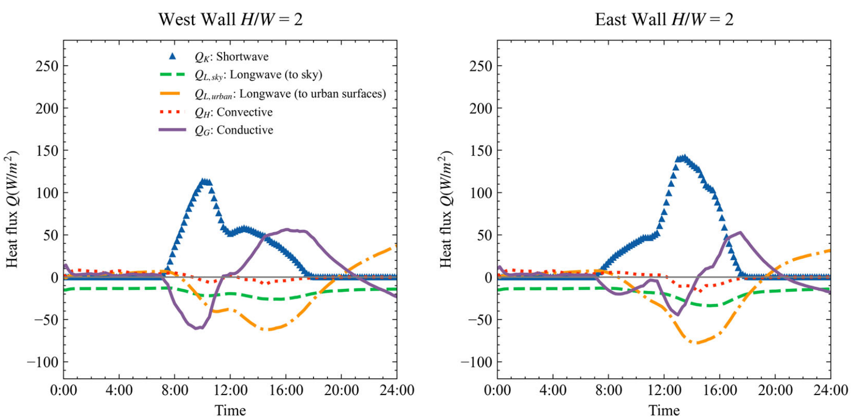

(b) $H/W = 2$

https://doi.org/10.5194/egusphere-2025-1485
Preprint. Discussion started: 19 May 2025

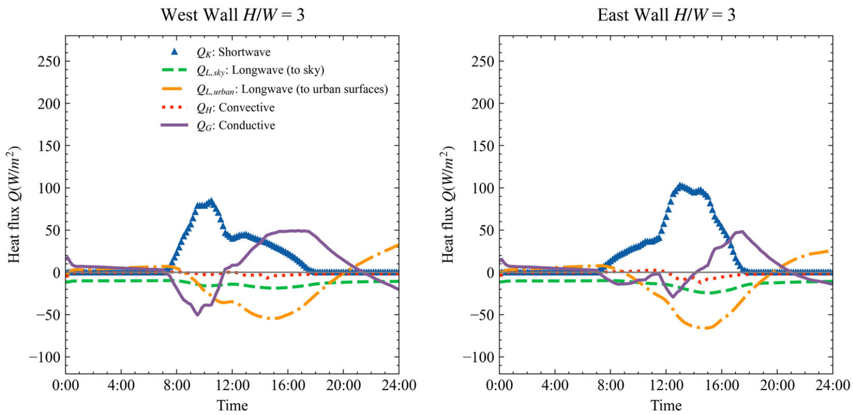

(c) $H/W = 3$

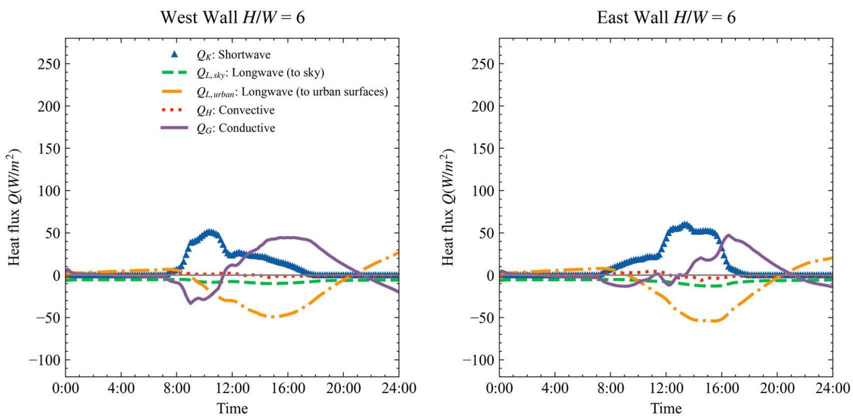

(d) $H/W = 6$

Figure 11: Diurnal heat fluxes from the simulation. The heat fluxes of shortwave (Q_K), longwave radiation (Q_L), convection (Q_H), and conduction (Q_G) are at the outer surface of walls.

4. Application to real urban configuration

To show how this model can be implemented in complex geometries, a neighborhood with 40 buildings is modeled. The building geometries are constructed by $.stl$ files with 2.3×10^4 triangular surface meshes. The surface temperatures are calculated on the grids. As a demonstration case, the complex

https://doi.org/10.5194/egusphere-2025-1485
Preprint. Discussion started: 19 May 2025

albedo of urban surfaces is ignored. A uniform albedo of 0.24 is used for all urban surfaces. The walls, roofs, and ground are assumed to be constructed by three layers of concrete. The layer thickness of walls and roofs is 10 cm. The total thickness of the ground is 35cm, with an adiabatic bottom boundary. The buildings are assumed to be naturally ventilated, with the indoor and outdoor air temperatures being the same. The thermal characteristics of concrete are assumed to be the same as in the SOMUCH experiment.

The surface temperatures are calculated in three steps: 1) calculate the solar radiative flux of each point by rMCRT; 2) calculate the view factors between the elements using rMCRT; 3) calculate the surface temperatures using Monte Carlo random walking. All three steps are processed in parallel on GPU. The weather data measured on 29th Jan 2021 during the SOMUCH experiment is used as the driving input. The surface temperatures are calculated from 0:00 to 24:00, with a time step of 30 minutes.

The simulation results are output in $.vtk$ format and visualized using ParaView. Fig. 12 shows the direct shortwave radiation and surface temperatures at 10:30 and 14:30. The movement of building shadows and their impact on surface temperatures are clearly observed in these contours. These contours demonstrate that this model can be applied to complex buildings in real urban areas.

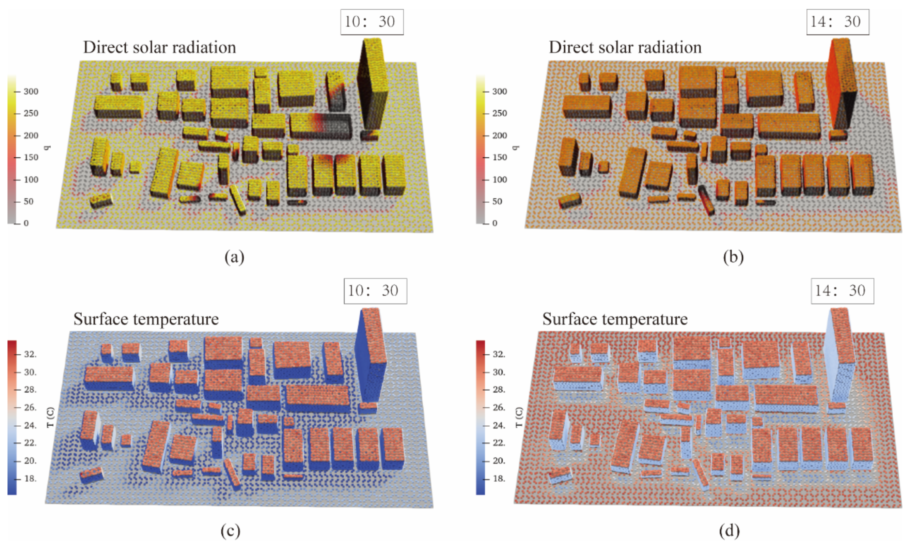

Figure 12: Radiation and temperature simulation results for complex building geometries. The direct shortwave radiation at 10:30 (a) and 14:30 (b). The surface temperatures at 10:30 (c) and 14:30 (d).

https://doi.org/10.5194/egusphere-2025-1485
Preprint. Discussion started: 19 May 2025

5. Limitations and future work

The first version focuses on the complex radiative exchange in densely built urban areas. The parameters and assumptions are validated against the idealized scaled outdoor experiment, which uses homogeneous building materials with consistent albedo and thermal characteristics. Glazing and green infrastructure are not included in this experiment. The SOMUCH project is currently measuring the impact of glass and green infrastructure. The next version will expand its capabilities to capture complex urban materials, such as urban trees, green walls, and glass curtain walls, to better represent real urban configurations. Other limitations include:

- All reflections are assumed to be Lambertian. While this assumption works well for the SOMUCH measurements, where concrete is used for all urban surfaces, it may not fully capture the reflective properties of other materials with different surface textures, such as glass or vegetation.
- The high-resolution wall temperature simulation still requires a significant amount of time to complete, even with parallel computation on GPUs. This is due to the large number of rays ($N = 10^6$) required for accurate solar radiation modeling. For each point, the simulation takes about 1 second to finish. However, as the number of test points increases, the overall computational time grows substantially.
- The dynamic indoor air temperature is not included in this model. It assumes that the indoor air temperature is equal to the outdoor air temperature for a natural ventilated room. This assumption may lead to discrepancies, particularly in situations where indoor temperatures differ from outdoor conditions due to factors such as heat sources, insulation, or limited ventilation.
- The participation of the urban atmosphere is ignored in this study. In the scaled measurements, longwave radiation travels much shorter distances to adjacent surfaces, which reduces the influence of atmospheric effects compared to real-world urban environments.

6. Conclusions

This study introduces a GPU-accelerated Urban Surface Temperature model (GUST), which solves the conduction-radiation-convection coupled heat transfer using Monte Carlo method. The GPU parallel computing is adopted to address the large computational demands of Monte Carlo method. This model

https://doi.org/10.5194/egusphere-2025-1485
Preprint. Discussion started: 19 May 2025

is validated with a scaled outdoor experiment (SOMUCH), which has a high spatial and temporal resolution.

The radiative heat flux is simulated using a reverse Monte Carlo Ray Tracing method, which allows for the accurate reproduction of multiple reflections in high-density urban areas. The sensitivity test shows that $10^5 \sim 10^6$ rays are required for each point to accurately model the shortwave radiation. This large amount of ray tracing can only be achieved using GPU parallel computing. The Monte Carlo method is also used to solve the couple heat transfer using random walking algorithms, which is suitable for GPU-based coding.

The comparison with the SOMUCH experiment shows that the transient surface temperatures on roofs, walls and the ground are well reproduced. A relatively large discrepancy is observed in cases with high building density, where the wall temperatures are highly sensitive to convective and longwave radiative fluxes. The surface energy balance analysis shows that longwave radiation exchange between urban surfaces plays a critical role across all building densities. In contrast, convective heat flux only plays a significant role in high-density cases. In future versions, the simulation of convective heat flux could be improved by simulating urban airflow.

Lastly, this model is implemented to solve the surface temperatures on complex urban buildings, which are composed of a total of 2.3×10^4 surface elements. The GPU allows simultaneous simulation of heat transfer and view factors across all elements, enabling high-fidelity simulations in real urban configurations with complex geometries. The current version focuses on the radiation-conduction-convection coupled heat transfer coupled in complex geometries. Future developments will prioritize the integration of complex glazing systems and green infrastructure in urban environments.

Code availability

The SOMUCH measurement data is available upon request. The development of GUST, model validation, and visualization in this study were conducted using Python 3.8 with CUDA. The source code, supporting data, and simulation results presented in this paper are archived on Zenodo at

https://doi.org/10.5194/egusphere-2025-1485
Preprint. Discussion started: 19 May 2025

https://doi.org/10.5281/zenodo.15074365 (Mei, 2025). Users are requested to contact the corresponding authors to obtain access to the code free of charge for research purposes under a collaboration agreement (meishj@mail.sysu.edu.cn).

Author contributions

SM designed the study, developed the code, conducted the analysis. SM and GC prepared the manuscript draft. GC and JH collected and shared SOMUCH measurements for the purpose of model validation. GC, JH and TS supported the model implementation and data analysis. All have read and accepted the manuscript for submission.

Acknowledgement

This research is supported by National Natural Science Foundation of China (Grant No. 42305076, W2421048, U2442212), Natural Science Foundation of Guangdong Province, China (Grant No. 2024A1515010173) and Overseas Postdoctoral Talents 2023 Programme (Grant No. BH2023009). Dr. Shuo-Jun Mei and Dr. Ting Sun are supported by an International Exchanges grant from the Royal Society (Grant No. IEC\NSFC\242040) and National Natural Science Foundation of China (Grant No. W2421048).

Appendix A. Indoor and outdoor air temperatures in SOMUCH measurement

The indoor and outdoor air temperatures at different levels in the SOMUCH measurement are plotted in Fig. A1. These air temperatures serve as input data for the validation cases.

https://doi.org/10.5194/egusphere-2025-1485
Preprint. Discussion started: 19 May 2025

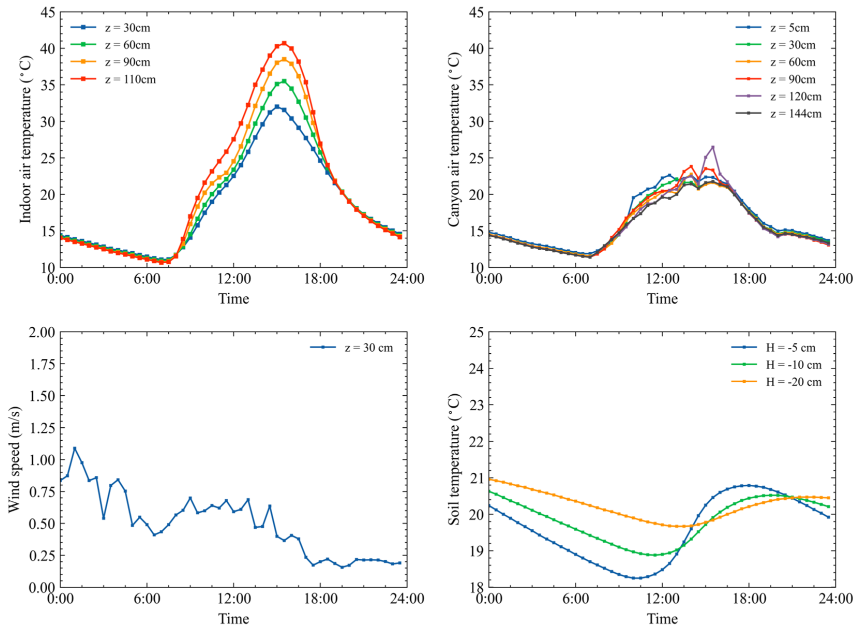

(a) $H/W = 1$

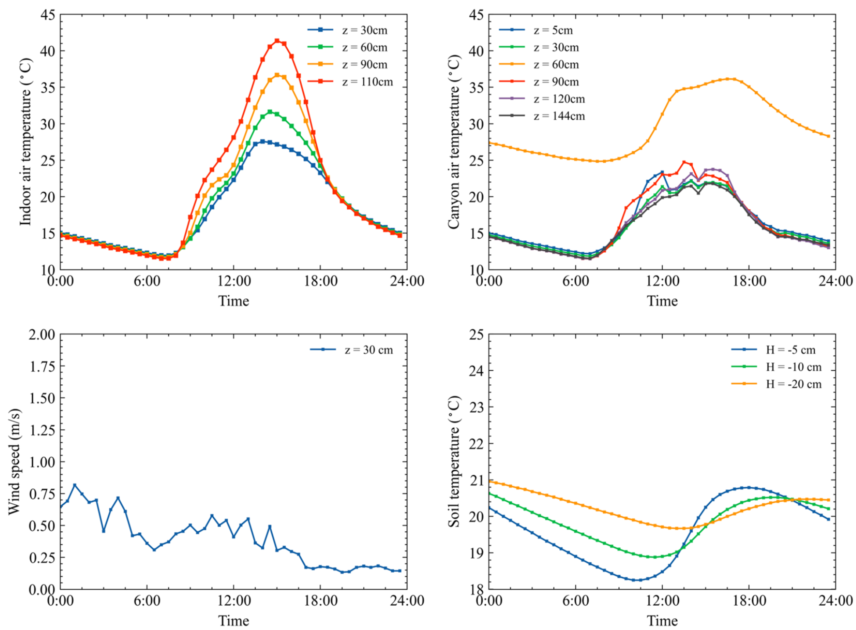

(b) $H/W = 2$

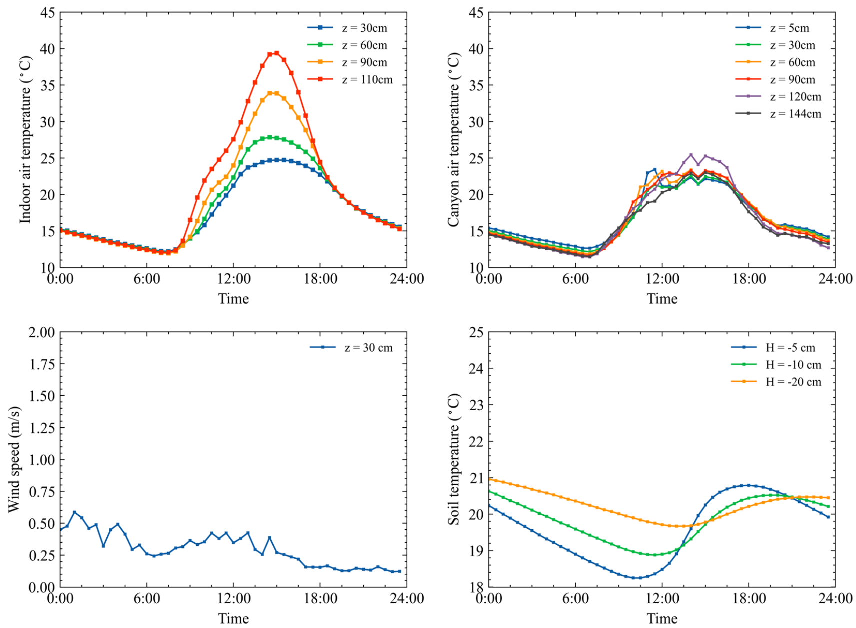
Indoor air temperature (°C)
z = 30cm
z = 60cm
z = 90cm
z = 110cm
Canyon air temperature (°C)
z = 5cm
z = 30cm
z = 60cm
z = 90cm
z = 120cm
z = 144cm
Wind speed (m/s)
z = 30 cm
Soil temperature (°C)
H = -5 cm
H = -10 cm
H = -20 cm
Time

(c) $H/W = 3$

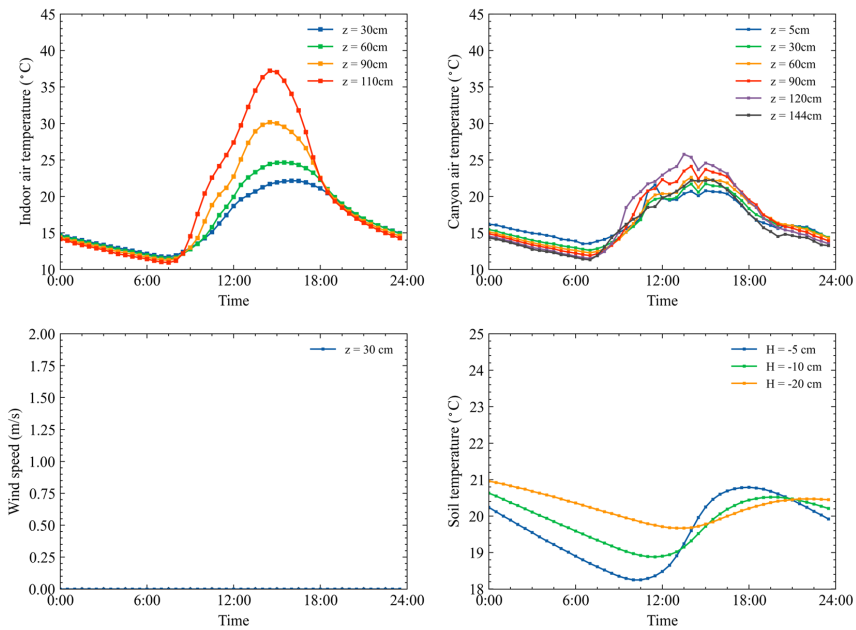
Indoor air temperature (°C)
z = 30cm
z = 60cm
z = 90cm
z = 110cm
Canyon air temperature (°C)
z = 5cm
z = 30cm
z = 60cm
z = 90cm
z = 120cm
z = 144cm
Wind speed (m/s)
z = 30 cm
Soil temperature (°C)
H = -5 cm
H = -10 cm
H = -20 cm
Time

(d) $H/W = 6$

Figure A1: Indoor, outdoor air temperatures, and wind speeds in street canyons that are measured on 29th Jan 2021. The wind speeds in the street canyon of *H*/*W* = 6 were not measured because the sonic anemometer cannot be installed in such a narrow street. The outdoor air temperatures measured at z = 60 cm in *H*/*W* = 2 are unusual, due to an instrument failure.

References

Bentham, T. and Britter, R.: Spatially averaged flow within obstacle arrays, Atmospheric Environment, 37, 2037-2043, https://doi.org/10.1016/S1352-2310(03)00123-7, 2003.

Caliot, C., d'Alençon, L., Blanco, S., Forest, V., Fournier, R., Hourdin, F., Retailleau, F., Schoetter, R., and Villefranque, N.: Coupled heat transfers resolution by Monte Carlo in urban geometry including direct and diffuse solar irradiations, International Journal of Heat and Mass Transfer, 222, 125139, https://doi.org/10.1016/j.ijheatmasstransfer.2023.125139, 2024.

Carmeliet, J. and Derome, D.: How to beat the heat in cities through urban climate modelling, Nature Reviews Physics, 6, 2-3, 10.1038/s42254-023-00673-1, 2024.

Chen, G., Mei, S.-J., Hang, J., Li, Q., and Wang, X.: URANS simulations of urban microclimates: Validated by scaled outdoor experiments, Building and Environment, 272, 112691, https://doi.org/10.1016/j.buildenv.2025.112691, 2025.

Ebi, K. L., Capon, A., Berry, P., Broderick, C., de Dear, R., Havenith, G., Honda, Y., Kovats, R. S., Ma, W., Malik, A., Morris, N. B., Nybo, L., Seneviratne, S. I., Vanos, J., and Jay, O.: Hot weather and heat extremes: health risks, The Lancet, 398, 698-708, https://doi.org/10.1016/S0140-6736(21)01208-3, 2021.

Eingrüber, N., Domm, A. S., Korres, W., and Schneider, K.: Simulation of the heat mitigation potential of unsealing measures in cities by parameterizing grass grid pavers for urban microclimate modelling with ENVI-met (V5), EGUsphere, 2024, 1-25, 10.5194/egusphere-2024-697, 2024.

Fan, Y., Zhao, Y., Torres, J. F., Xu, F., Lei, C., Li, Y., and Carmeliet, J.: Natural convection over vertical and horizontal heated flat surfaces: A review of recent progress focusing on underpinnings and implications for heat transfer and environmental applications, Physics of Fluids, 33, 101301, 10.1063/5.0065125, 2021.

Feng, J., Gao, K., Khan, H., Ulpiani, G., Vasilakopoulou, K., Young Yun, G., and Santamouris, M.: Overheating of Cities: Magnitude, Characteristics, Impact, Mitigation and Adaptation, and Future Challenges, Annual Review of Environment and Resources, 48, 651-679, https://doi.org/10.1146/annurev-environ-112321-093021, 2023.

Forouzandeh, A.: Prediction of surface temperature of building surrounding envelopes using holistic microclimate ENVI-met model, Sustainable Cities and Society, 70, 102878,

https://doi.org/10.5194/egusphere-2025-1485
Preprint. Discussion started: 19 May 2025

https://doi.org/10.1016/j.scs.2021.102878, 2021.

Grimmond, C. S. B. and Oke, T. R.: Aerodynamic properties of urban areas derived from analysis of surface form, Journal of Applied Meteorology, 38, 1262, 10.1175/1520-0450(1999)038<1262:APOUAD>2.0.CO;2, 1999.

Hang, J. and Chen, G.: Experimental study of urban microclimate on scaled street canyons with various aspect ratios, Urban Climate, 46, 101299, https://doi.org/10.1016/j.uclim.2022.101299, 2022.

Hang, J., Zeng, L., Li, X., and Wang, D.: Evaluation of a single-layer urban energy balance model using measured energy fluxes by scaled outdoor experiments in humid subtropical climate, Building and Environment, 254, 111364, https://doi.org/10.1016/j.buildenv.2024.111364, 2024.

Hang, J., Lu, M., Ren, L., Dong, H., Zhao, Y., and Zhao, N.: Cooling performance of near-infrared and traditional high-reflective coatings under various coating modes and building area densities in 3D urban models: Scaled outdoor experiments, Sustainable Cities and Society, 121, 106200, https://doi.org/10.1016/j.scs.2025.106200, 2025.

Hénon, A., Mestayer, P. G., Lagouarde, J.-P., and Voogt, J. A.: An urban neighborhood temperature and energy study from the CAPITOUL experiment with the Solene model, Theoretical and Applied Climatology, 110, 197-208, 10.1007/s00704-012-0616-z, 2012.

Imbert, C., Bhattacharjee, S., and Tencar, J.: Simulation of urban microclimate with SOLENE-microclimat: an outdoor comfort case study, Proceedings of the Symposium on Simulation for Architecture and Urban Design, Delft, Netherlands2018.

Kondo, A., Ueno, M., Kaga, A., and Yamaguchi, K.: The Influence Of Urban Canopy Configuration On Urban Albedo, Boundary-Layer Meteorology, 100, 225-242, 10.1023/A:1019243326464, 2001.

Krayenhoff, E. S. and Voogt, J. A.: A microscale three-dimensional urban energy balance model for studying surface temperatures, Boundary-Layer Meteorology, 123, 433-461, 10.1007/s10546-006-9153-6, 2007.

Manoli, G., Fatichi, S., Schläpfer, M., Yu, K., Crowther, T. W., Meili, N., Burlando, P., Katul, G. G., and Bou-Zeid, E.: Magnitude of urban heat islands largely explained by climate and population, Nature, 573, 55-60, 10.1038/s41586-019-1512-9, 2019.

Mei, S.-J.: GUST1.0: A GPU-accelerated 3D Urban Surface Temperature Model (1.0), Zenodo [dataset], https://doi.org/10.5281/zenodo.15074365, 2025.

Owens, S. O., Majumdar, D., Wilson, C. E., Bartholomew, P., and van Reeuwijk, M.: A conservative immersed boundary method for the multi-physics urban large-eddy simulation model uDALES v2.0, Geoscientific Model Development, 17, 6277-6300, 10.5194/gmd-17-6277-2024, 2024.

Reindl, D. T., Beckman, W. A., and Duffie, J. A.: Diffuse fraction correlations, Solar Energy, 45, 1-7, https://doi.org/10.1016/0038-092X(90)90060-P, 1990.

Resler, J., Krc, P., Belda, M., Jurus, P., Benesova, N., Lopata, J., Vlcek, O., Damaskova, D., Eben, K., Derbek, P., Maronga, B., and Kanani-Suhring, F.: PALM-USM v1.0: A new urban surface model integrated into the PALM large-eddy simulation model, Geoscientific Model Development, 10, 3635-3659, 10.5194/gmd-10-3635-2017, 2017.

Rodriguez, A., Lecigne, B., Wood, S., Carmeliet, J., Kubilay, A., and Derome, D.: Optimal representation of tree foliage for local urban climate modeling, Sustainable Cities and Society, 115, 105857, https://doi.org/10.1016/j.scs.2024.105857, 2024.

Salim, M. H., Schlünzen, K. H., Grawe, D., Boettcher, M., Gierisch, A. M. U., and Fock, B. H.: The microscale obstacle-resolving meteorological model MITRAS v2.0: model theory, Geoscientific Model Development, 11, 3427-3445, 10.5194/gmd-11-3427-2018, 2018.

Schoetter, R., Caliot, C., Chung, T.-Y., Hogan, R. J., and Masson, V.: Quantification of Uncertainties of Radiative Transfer Calculation in Urban Canopy Models, Boundary-Layer Meteorology, 189, 103-138, 10.1007/s10546-023-00827-9, 2023.

Talebi, S., Gharehbash, K., and Jalali, H. R.: Study on random walk and its application to solution of heat conduction equation by Monte Carlo method, Progress in Nuclear Energy, 96, 18-35, https://doi.org/10.1016/j.pnucene.2016.12.004, 2017.

Toparlar, Y., Blocken, B., Vos, P., van Heijst, G. J. F., Janssen, W. D., van Hooff, T., Montazeri, H., and Timmermans, H. J. P.: CFD simulation and validation of urban microclimate: A case study for Bergpolder Zuid, Rotterdam, Building and Environment, 83, 79-90, https://doi.org/10.1016/j.buildenv.2014.08.004, 2015.

Tregan, J. M., Amestoy, J. L., Bati, M., Bezian, J.-J., Blanco, S., Brunel, L., Caliot, C., Charon, J., Cornet, J.-F., Coustet, C., d'Alençon, L., Dauchet, J., Dutour, S., Eibner, S., El Hafi, M., Eymet, V., Farges, O., Forest, V., Fournier, R., Galtier, M., Gattepaille, V., Gautrais, J., He, Z., Hourdin, F., Ibarrart, L., Joly, J.-L., Lapeyre, P., Lavieille, P., Lecureux, M.-H., Lluc, J., Miscevic, M., Mourtaday, N., Nyffenegger-Péré, Y., Pelissier, L., Penazzi, L., Piaud, B., Rodrigues-Viguier, C., Roques, G., Roger, M., Saez, T., Terrée, G., Villefranque, N., Vourc'h, T., and Yaacoub, D.: Coupling radiative, conductive and convective heat-transfers in a single Monte Carlo algorithm: A general theoretical framework for linear situations, PLoS One, 18, e0283681, 10.1371/journal.pone.0283681, 2023.

Tuholske, C., Caylor, K., Funk, C., Verdin, A., Sweeney, S., Grace, K., Peterson, P., and Evans, T.: Global urban population exposure to extreme heat, Proceedings of the National Academy of Sciences of the United States of America, 118, e2024792118, doi:10.1073/pnas.2024792118, 2021.

Villefranque, N., Hourdin, F., d'Alençon, L., Blanco, S., Boucher, O., Caliot, C., Coustet, C., Dauchet, J., El Hafi, M., Eymet, V., Farges, O., Forest, V., Fournier, R., Gautrais, J., Masson, V., Piaud, B., and Schoetter, R.: The "teapot in a city": A paradigm shift in urban climate modeling, Science Advances, 8, eabp8934, doi:10.1126/sciadv.abp8934, 2022.

Voogt, J. A. and Oke, T. R.: Effects of urban surface geometry on remotely-sensed surface temperature, International Journal of Remote Sensing, 19, 895-920, 10.1080/014311698215784, 1998.

Wang, K., Li, Y., Li, Y., and Lin, B.: Stone forest as a small-scale field model for the study of urban climate, International Journal of Climatology, 38, 3723-3731, https://doi.org/10.1002/joc.5536, 2018.

Wang, W., Wang, X., and Ng, E.: The coupled effect of mechanical and thermal conditions on pedestrian-level ventilation in high-rise urban scenarios, Building and Environment, 191, 107586, https://doi.org/10.1016/j.buildenv.2021.107586, 2021.

Wu, Z., Shi, Y., Ren, L., and Hang, J.: Scaled outdoor experiments to assess impacts of tree evapotranspiration and shading on microclimates and energy fluxes in 2D street canyons, Sustainable Cities and Society, 108, 105486, https://doi.org/10.1016/j.scs.2024.105486, 2024.

Yang, X. and Li, Y.: Development of a Three-Dimensional Urban Energy Model for Predicting and Understanding Surface Temperature Distribution, Boundary-Layer Meteorology, 149, 303-321, 10.1007/s10546-013-9842-x, 2013.

Yang, X. and Li, Y.: The impact of building density and building height heterogeneity on average urban albedo and street surface temperature, Building and Environment, 90, 146-156, https://doi.org/10.1016/j.buildenv.2015.03.037, 2015.

Yoshida, K., Miwa, S., Yamaki, H., and Honda, H.: Analyzing the impact of CUDA versions on GPU applications, Parallel Computing, 120, 103081, https://doi.org/10.1016/j.parco.2024.103081, 2024.

Yuan, C., Adelia, A. S., Mei, S., He, W., Li, X.-X., and Norford, L.: Mitigating intensity of urban heat island by better understanding on urban morphology and anthropogenic heat dispersion, Building and Environment, 176, 106876, https://doi.org/10.1016/j.buildenv.2020.106876, 2020.

Yuan, C., Shan, R., Zhang, Y., Li, X.-X., Yin, T., Hang, J., and Norford, L.: Multilayer urban canopy modelling and mapping for traffic pollutant dispersion at high density urban areas, Science of The Total Environment, 647, 255-267, https://doi.org/10.1016/j.scitotenv.2018.07.409, 2019.